First-principles simulations of exciton diffusion in organic semiconductors

Xu Zhang, Zi Li, and Gang Lu

Department of Physics and Astronomy, California State University Northridge, Northridge, California 91330-8268, USA

(Received 22 September 2011; published 22 December 2011)

Exciton diffusion is crucial for the performance of organic semiconductors in photovoltaic and solid state lighting applications. We propose a first-principles approach that can predict exciton dynamics in organic semiconductors. The method is based on time-dependent density functional theory to describe the energy and many-body wave functions of excitons. Nonadiabatic *ab initio* molecular dynamics is used to calculate phonon-assisted transition rates between localized exciton states. Using Monte Carlo simulations, we determine the exciton diffusion length, lifetime, diffusivity, and harvesting efficiency in poly(3-hexylthiophene) polymers at different temperatures, which agree very well with the experiments. We find that exciton diffusion is primarily determined by the density of states of low-energy excitons. A widely speculated diffusion mechanism, namely an initial downhill migration followed by thermally activated migration, is confirmed and elucidated by the simulations. Some general guidelines for designing more efficient organic solar cells are obtained from the simulations.

DOI: 10.1103/PhysRevB.84.235208 PACS number(s): 72.80.Le, 71.10.Li, 71.15.Pd

I. INTRODUCTION

Exciton diffusion is of great importance to the performance of organic optoelectronic devices, including organic photovoltaics and solid state lighting. For instance, in organic solar cells high exciton mobility is desirable because excitons have to migrate to the donor/acceptor interfaces for charge separation within their lifetimes.[1] In contrast, in electroluminescent devices such as organic light emitting diodes, efficient exciton diffusion would increase the probability that the excitons reach the quenching sites, contributing to the degradation of the devices' performance.[2] Therefore, the ability to control exciton dynamics in organic semiconductors, either by facilitating or hindering exciton diffusion, is crucial to the design of the optoelectronic devices. However, such an ability hinges upon the fundamental understanding of the exciton diffusion mechanism. In addition, it is highly desirable to be able to predict exciton diffusion so that promising materials can be identified or prescreened computationally prior to their synthesis. Here we propose a first-principles approach that can predict exciton dynamics in organic semiconductors and elucidate the exciton diffusion mechanism. Such a theoretical tool can greatly expand our capability to rationally design more efficient organic optoelectronic materials.

Earlier theoretical work has employed the Forster-type energy transfer model to calculate exciton transition rates based on the empirical Miller-Abrahams form;[3,4] these approaches are not material specific and contain empirical parameters, thus they have a limited predictive power. To be more predictive, quantum chemical methods have been put forward in conjunction with a distributed monopole model to determine the exciton transition rates employing the Fermi golden rule.[5–8] However, all these methods assume a Gaussian distribution of exciton density of states, as well as perturbation theories and harmonic approximations, whose validity is not generally established. More importantly, none of the methods above has considered explicitly the many-body wave functions and energy levels of the excitons—both are important for exciton dynamics. The proposed approach overcomes these deficiencies and is based on the time-dependent density functional theory (TDDFT)[9] to describe exciton states, including energy levels and many-body wave functions. The nonadiabatic *ab initio* molecular dynamics (MD)[10,11] is used to determine the phonon-assisted transition rates between localized exciton states. In conjunction with the Monte Carlo method, this approach can simulate exciton dynamics in semiconducting polymers at different temperatures.

In this paper, we will study exciton diffusion in conjugate polymer poly(3-hexylthiophene) (P3HT), which is the donor material in the state-of-the-art bulk heterojunction solar cells, reaching the power conversion efficiency of 5–7% (Refs. 12–14). The knowledge gained from this study is expected to be translated to other organic semiconductors as well. In realistic photovoltaic devices—either pure P3HT films or the bulk heterojunctions—there always exist amorphous interphases[15] and interfaces;[16] since the exciton diffusion in these amorphous phases limits the overall exciton dynamics, in this paper we will focus on exciton diffusion in amorphous P3HT.

II. METHODOLOGY

We have developed a theoretical framework that can predict the exciton dynamics including exciton diffusion length, diffusion lifetime, diffusivity, and harvesting efficiency from first-principles simulations. The multiscale framework integrates *ab initio* Born-Oppenheimer MD, TDDFT (with range-separated exchange-correlation functional), nonadiabatic *ab initio* MD and Monte Carlo simulations; the coherent integration of the computational components is summarized in the flowchart shown in Fig. 1, which will be elaborated in the following.

A. Determining exciton states

We first carry out *ab initio* MD based on the Kohn-Sham (KS) DFT to capture the effect of static and dynamic disorder on the ground state electronic structure. At each MD time step, we determine the energy levels and many-body wave functions of the excitons from the KS eigenvalues $\epsilon_{i\sigma}$ and eigenfunctions

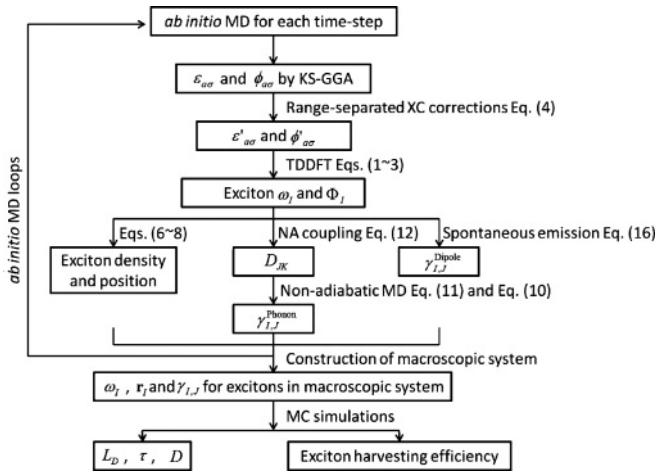

FIG. 1. Flowchart of the multiscale simulation framework.

$\phi_{i\sigma}$ following the TDDFT formulation of Casida.[17] To this end, we solve the following non-Hermitian pseudo-eigenvalue equation at each MD step:

$$\begin{pmatrix} \mathbf{A} & \mathbf{B} \\ \mathbf{B}^* & \mathbf{A}^* \end{pmatrix} \begin{pmatrix} \mathbf{X}_I \\ \mathbf{Y}_I \end{pmatrix} = \omega_I \begin{pmatrix} \mathbf{1} & \mathbf{0} \\ \mathbf{0} & -\mathbf{1} \end{pmatrix} \begin{pmatrix} \mathbf{X}_I \\ \mathbf{Y}_I \end{pmatrix}, \tag{1}$$

where the pseudo-eigenvalue ω_I is the Ith exciton energy level; the matrix elements of $\mathbf{A}$ and $\mathbf{B}$ in the basis of KS states $\{ij\sigma\}$ are given by

$$\begin{aligned} A_{ij\sigma,kl\tau} &= \delta_{i,k}\delta_{j,l}\delta_{\sigma,\tau}(\epsilon_{j\sigma} - \epsilon_{i\sigma}) + K_{ij\sigma,kl\tau}, \\ B_{ij\sigma,kl\tau} &= K_{ij\sigma,lk\tau}. \end{aligned} \tag{2}$$

Here K is the coupling matrix where indices i and k indicate the occupied orbitals, and j and l represent the virtual orbitals. According to the assignment ansatz of Casida, the many-body wave function of the exciton state I, Φ_I is written as

$$\Phi_I \approx \sum_{ij\sigma} \frac{\mathbf{X}_{I,ij\sigma} + \mathbf{Y}_{I,ij\sigma}}{\sqrt{\omega_I}} \hat{a}^\dagger_{j\sigma}\hat{a}_{i\sigma}\Phi_0, \tag{3}$$

where $\hat{a}_{i\sigma}$ is the annihilation operator acting on the ith KS orbital with spin σ, and Φ_0 is the ground state many-body wave function taken to be the single Slater determinant (SD) of the occupied KS orbitals.

To describe charge transfer excitations accurately, we incorporate a range-separated exchange-correlation (XC) functional[18,19] into the TDDFT formalism. The range-separated XC functional combines the Hartree-Fock (HF) exchange to reproduce the $-1/r$ asymptotic behavior of the exchange potential at a long range and the generalized gradient approximation (GGA) at a short range; it has been shown to describe $\pi \to \pi^*$ transitions accurately in conjugated polymers.[20] The range-separated functional can be expressed as $E'_{\rm xc} = E_{\rm xc,GGA} - E^{\rm LR}_{\rm x,GGA} + E^{\rm LR}_{\rm x,HF}$, where $E_{\rm xc,GGA}$ is the GGA energy functional, $E^{\rm LR}_{\rm x,GGA}$ is the long-range part of the GGA exchange energy functional, and $E^{\rm LR}_{\rm x,HF}$ is the long-range part of the Hartree-Fock exchange integral. We have recently proposed an efficient range-separated XC method[21] which is used to correct the KS eigenvalues and eigenfunctions in the TDDFT formalism. These corrections are carried out at each MD step as indicated in the flowchart Fig. 1. In the following, the superscript prime is denoted for quantities that are corrected by the range-separated XC functional from the GGA results. Indices a and b run over occupied orbitals (i) and virtual orbitals (j). In the basis of KS eigenfunctions $\phi_{a\sigma}$, the corrected Hamiltonian matrix elements are[21]

$$\begin{aligned} \hat{H}'_{ab\sigma} &= \epsilon_{a\sigma}\delta_{ab} - \int \phi^*_{b\sigma}(\mathbf{r}) V^{{\rm LR},\sigma}_{\rm x,GGA}[\rho_\sigma(\mathbf{r}),\rho_\tau(\mathbf{r})]\phi_{a\sigma}(\mathbf{r})d\mathbf{r} \\ &\quad - \sum_c^{\rm occ}\left[\phi^*_{b\sigma}\phi_{c\sigma}\left|\frac{{\rm erf}(\mu r)}{r}\right|\phi^*_{c\sigma}\phi_{a\sigma}\right]. \end{aligned} \tag{4}$$

Here $V^{{\rm LR},\sigma}_{\rm x,GGA}$ is the long-range part of the GGA exchange potential for spin σ; ρ_σ is the charge density of spin σ calculated as $\rho_\sigma(\mathbf{r}) = \sum_c^{\rm occ}\phi^*_{c\sigma}(\mathbf{r})\phi_{c\sigma}(\mathbf{r})$; and the Coulomb product $[f|\frac{1}{r}|g] = \int\int \frac{f(\mathbf{r}_1)g(\mathbf{r}_2)}{|\mathbf{r}_1-\mathbf{r}_2|}d\mathbf{r}_1 d\mathbf{r}_2$ has been introduced here. μ is the range-separation parameter chosen as 0.62 Å^{-1} which has been well validated.[18,21] The index c includes all occupied orbitals. The KS eigenvalue $\epsilon'_{a\sigma}$ and eigenfunction $\phi'_{a\sigma}$ can be obtained via a direct diagonalization of the Hamiltonian matrix $\hat{H}'$, and is used in the TDDFT calculation with Eq. (1). With the corrected eigenvalues and eigenfunctions, the coupling matrix K is given by

$$\begin{aligned} K_{ij\sigma,kl\tau} &= \left[\phi'^*_{i\sigma}\phi'_{j\sigma}\left|\frac{1}{r}\right|\phi'_{k\tau}\phi'^*_{l\tau}\right] \\ &\quad - \delta_{\sigma\tau}\left[\phi'^*_{i\sigma}\phi'_{k\tau}\left|\frac{{\rm erf}(\mu r)}{r}\right|\phi'_{j\sigma}\phi'^*_{l\tau}\right] \\ &\quad + \int \phi'^*_{i\sigma}(\mathbf{r})\phi'_{j\sigma}(\mathbf{r})\frac{\delta^2\left(E_{\rm xc,GGA} - E^{\rm LR}_{\rm x,GGA}\right)}{\delta\rho_\sigma(\mathbf{r})\delta\rho_\tau(\mathbf{r}')} \\ &\quad \times \phi'_{k\tau}(\mathbf{r}')\phi'^*_{l\tau}(\mathbf{r}')d\mathbf{r}d\mathbf{r}'. \end{aligned} \tag{5}$$

Thus in the calculation of Eq. (2), the eigenvalues $\epsilon_{i\sigma}$ should be replaced by $\epsilon'_{i\sigma}$, with the coupling matrix determined by Eq. (5).

B. Exciton charge density and spatial positions

Given the many-body wave functions, one can determine the charge density of the exciton. Here we consider the spin-restricted case to focus on singlet excitons, although the same approach can be generalized to triplet excitons. In an N-electron system, the density operator is $\hat{\rho}(\mathbf{r}) = \sum_{n=1}^N \delta(\mathbf{r} - \mathbf{r}_n)$. Hence the charge density of the Ith excited state can be derived as

$$\begin{aligned} \langle\Phi_I|\hat{\rho}(\mathbf{r})|\Phi_I\rangle &= \rho_0(\mathbf{r}) + \sum_{i,jj'} z^*_{I,ij}z_{I,ij'}\phi^*_j(\mathbf{r})\phi_{j'}(\mathbf{r}) \\ &\quad - \sum_{ii',j} z^*_{I,ij}z_{I,i'j}\phi^*_{i'}(\mathbf{r})\phi_i(\mathbf{r}), \end{aligned} \tag{6}$$

where $\rho_0(\mathbf{r}) = \sum_c^{\rm occ}\phi^*_c(\mathbf{r})\phi_c(\mathbf{r})$ is the charge density of the KS ground state and $z_{I,ij} = (\mathbf{X}_{I,ij} + \mathbf{Y}_{I,ij})/\sqrt{\omega_I}$. Since an exciton is a bond state of a quasi-electron and a quasihole, the second term on the right-hand side of Eq. (6) represents the charge density of the quasi-electron and the third term corresponds to the charge density of the quasihole. This identification is consistent with the fact that the index i refers to the occupied orbitals (holes), while j refers to the virtual orbitals (electrons) as in Eq. (2). Therefore one can represent the charge density of

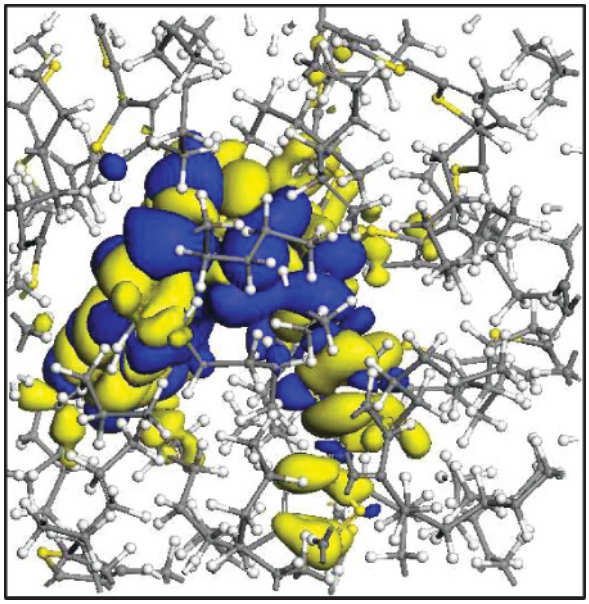

FIG. 2. (Color online) Charge density of the lowest energy exciton in amorphous P3HT. The computational box is of a dimension of 1.8 nm. The blue (yellow) isosurface illustrates the charge density distribution at $+(-)\,0.005$ Å^{-3}. The positive (negative) charge density corresponds to the quasi-electron (hole). The gray, white, and yellow spheres denote C, H, and S atoms, respectively.

an exciton by the corresponding densities of its quasi-electron and quasihole. This representation is convenient because it reduces the many-body object (the charge density of the exciton) to the single-particle densities, which can be easily visualized and analyzed. For amorphous P3HT, we find that the quasi-electron and quasihole are localized on the *same* P3HT chain shown in Fig. 2, consistent with experimental observation of intrachain Frenkel excitons.[22–24] With increased crystalline order, we find that the excitons acquire both intrachain and interchain characteristics, also agreeing with the experimental observations.[24] In addition, we estimate that the first excitation energy of the crystalline P3HT ranges from 1.5 to 2.4 eV, comparing well to the corresponding experimental value of ∼2.0 eV (Ref. 25). For the crystalline P3HT, we find that the first excitation energy depends sensitively on the stacking order of $\pi-\pi$ wave functions, and the two numbers cited above correspond to two opposite stacking orders. Overall, the TDDFT calculations provide an accurate description of the static properties of excitons in P3HT.

To simulate exciton diffusion, it is often useful to define the spatial positions of the excitons. With the position operator $\hat{\mathbf{r}} = \sum_{n=1}^{N} \mathbf{r}_n$, the position of the exciton I in the N-electron system is given by

$$\langle \Phi_I|\hat{\mathbf{r}}|\Phi_I\rangle = \int \rho_0(\mathbf{r})\mathbf{r}d\mathbf{r} + \sum_{i,jj'} z^*_{I,ij} z_{I,ij'} \langle \phi_j|\mathbf{r}|\phi_{j'}\rangle - \sum_{ii',j} z^*_{I,ij} z_{I,i'j} \langle \phi_{i'}|\mathbf{r}|\phi_i\rangle. \quad (7)$$

On the right-hand side of Eq. (7), the first term is the sum of all electron positions in the ground state; the second (third) term corresponds to the position of the quasi-electron $\mathbf{r}_e$ (quasihole $\mathbf{r}_h$). We can thus define the position of the exciton I $\mathbf{r}_{\rm ex}$ as

$$\mathbf{r}_{\rm ex} = \frac{\mathbf{r}_e + \mathbf{r}_h}{2}. \quad (8)$$

Again the advantage of this definition is to relate the many-body quantity of the exciton position with single-particle quantities ($\mathbf{r}_e$ and $\mathbf{r}_h$).

C. Exciton transition rates

Next, we determine phonon-assisted transition rates and the spontaneous emission rates of the excitons. We attribute exciton diffusion to the phonon-assisted transitions, including the adiabatic evolution of the excited states and the nonadiabatic hopping between the excited states. The thermal fluctuations of the ions could lead to an overlap between the exciton states in space and energy, and thus promote exciton transitions between the localized exciton states. Since these transitions can be nonadiabatic, the nonadiabatic *ab initio* molecular dynamics is used to describe the phonon-assisted transitions. During a molecular dynamics trajectory, the time-dependent many-body wave function of the exciton state $\Psi(t)$ can be expanded by a linear combination of a complete basis set consisting of the adiabatic ground state and the excited states $\Phi_I[\mathbf{R}(t)]$ at the present ionic positions $\mathbf{R}(t)$:

$$\Psi(t) = \sum_{I=0}^{\infty} C_I(t)\Phi_I[\mathbf{R}(t)], \quad (9)$$

where $C_I(t)$ is the expansion coefficient. Let the exciton start in a pure state I at $t=0$ (i.e., $\Psi(0)=\Phi_I[\mathbf{R}(0)]$) then the coefficient $C_J(t)$ in Eq. (9) can be labeled as $C_J^{(I)}(t)$ with the initial condition that $C_J^{(I)}(0)=\delta_{I,J}$. At $t>0$, ions move and $\Psi(t)$ becomes a mixed state. Therefore $|C_J^{(I)}(t)|^2$ represents the probability that the exciton makes a transition from state I to state J during a small time interval of δt (in this case $\delta t = t-0$). The phonon-assisted exciton transition rate from the state I to J, $\gamma_{I,J}^{\rm Phonon}$ is thus given by

$$\gamma_{I,J}^{\rm Phonon} = \left\langle \frac{\left|C_J^{(I)}(t)\right|^2}{t} \right\rangle_{\delta t}. \quad (10)$$

The average is taken over a short MD trajectory of δt. Here we use $\delta t = 100$ fs to determine the phonon-assisted transition rates. The evolution of $C_J^{(I)}(t)$ can be determined from the nonadiabatic *ab initio* molecular dynamics at each time step. Substituting Eq. (9) into the time-dependent Schrödinger equation, one arrives at the following equation involving the expansion coefficient $C_J(t)$:

$$\frac{\partial}{\partial t}C_J(t) = -\sum_K C_K(t)\left(\frac{i}{\hbar}\omega_K\delta_{JK} + D_{JK}\right). \quad (11)$$

A standard second-order finite-difference method with a time-step of 10^{-3} fs is employed to propagate the coefficient $C_J(t)$. And D_{JK} is the nonadiabatic coupling between two many-body electronic states J and K,

$$D_{JK} \equiv \langle \Phi_J|\nabla_{\mathbf{R}}|\Phi_K\rangle \cdot \frac{d\mathbf{R}}{dt} = \langle \Phi_J|\frac{\partial}{\partial t}|\Phi_K\rangle. \quad (12)$$

Substituting Eq. (3) into Eq. (12), we can obtain D_{JK} as

$$D_{JK} = \sum_{ii'jj'} z^*_{J,ij} z_{K,i'j'} \langle \Phi_{ij} | \frac{\partial}{\partial t} | \Phi_{i'j'} \rangle = \sum_{i,j\neq j'} z^*_{J,ij} z_{K,ij'} d_{jj'} - \sum_{i\neq i',j} z^*_{J,ij} z_{K,i'j} d_{i'i}, \quad (13)$$

where $\Phi_{ij} = \hat{a}^\dagger_j \hat{a}_i \Phi_0$ is a single SD of the KS orbitals, promoting an electron from an occupied state i to a virtual state j. $d_{jk} = \langle \phi_j | \frac{\partial}{\partial t} | \phi_k \rangle$ is the nonadiabatic coupling between the KS orbitals. One can show that

$$\langle \Phi_{ij} | \frac{\partial}{\partial t} | \Phi_{i'j'} \rangle = \begin{cases} 0, & \text{if } i = i' \text{ and } j = j', \\ d_{jj'}, & \text{if } i = i' \text{ and } j \neq j', \\ 0, & \text{if } i \neq i' \text{ and } j \neq j', \\ -d_{i'i}, & \text{if } i \neq i' \text{ and } j = j', \end{cases} \quad (14)$$

where $d_{ii} = 0$ has been used. Hence $\langle \Phi_{ij} | \frac{\partial}{\partial t} | \Phi_0 \rangle = d_{ji}$, and the nonadiabatic coupling between the exciton state J and the ground state is obtained as

$$D_{J0} = \sum_{i,j} z^*_{J,ij} d_{ji}. \quad (15)$$

Although the nonadiabatic coupling between the ground state and the excited states D_{J0} can be rigorously determined by TDDFT,[26] there is no such rigorous formulation for the nonadiabatic coupling between the excited states, therefore the approximate many-body wave functions in Eq. (3) have to be used in calculating Eq. (12).

Excitons can decay from a higher energy to a lower energy or even to the ground state (i.e., exciton annihilation) through the so-called spontaneous emission mechanism. Based on the transition dipole moment approximation, we can estimate the spontaneous emission rate between two exciton states as

$$\gamma^{\text{Dipole}}_{I,J} = \frac{4n(\omega_I - \omega_J)^3 |\langle \Phi_I | \hat{\mathbf{r}} | \Phi_J \rangle|^2}{3c^3}, \quad (16)$$

where c is the vacuum speed of light and n is the refractive index which takes a value of 1.5 for P3HT (Ref. 27). Similar to Eq. (7), the transition dipole moment can be evaluated as

$$\langle \Phi_I | \hat{\mathbf{r}} | \Phi_J \rangle = \sum_{i,jj'} z^*_{I,ij} z_{J,ij'} \langle \phi_j | \mathbf{r} | \phi_{j'} \rangle - \sum_{ii',j} z^*_{I,ij} z_{J,i'j} \langle \phi_{i'} | \mathbf{r} | \phi_i \rangle, \quad (17)$$

where I and J are the exciton states, and

$$\langle \Phi_I | \hat{\mathbf{r}} | \Phi_0 \rangle = \sum_{i,j} z^*_{I,ij} \langle \phi_j | \mathbf{r} | \phi_i \rangle, \quad (18)$$

represents the dipole moment between the exciton state I and the ground state.

Although the spontaneous emission contributes only to the energy downhill transitions, the phonon-assisted transitions could take place both downhill and uphill. To ensure a detailed balance, the thermal equilibrium transition rate $\gamma_{I,J}$ can be defined as[28]

$$\gamma_{I,J} = \begin{cases} \gamma^{\text{Phonon}}_{I,J} \exp\left(-\frac{\omega_J - \omega_I}{k_B T}\right), & \text{if } \omega_J \geqslant \omega_I, \\ \gamma^{\text{Phonon}}_{I,J} + \gamma^{\text{Dipole}}_{I,J}, & \text{if } \omega_J < \omega_I, \end{cases} \quad (19)$$

where k_B is the Boltzmann constant and T is temperature.

D. Construction of macroscopic system and Monte Carlo simulations

To examine exciton diffusion in a length scale that is relevant to the experiments, we divide the entire "macroscopic" system of interest into $L_x \times L_y \times L_z$ cubes; each cube should be chosen as large as computationally feasible, but at minimum the cube should accommodate the localized wave functions of the quasi-electron and the quasihole. The *ab initio* MD simulation is carried out for one of the cubes, termed home cube; the KS energy and wave functions obtained along the MD trajectories are used to construct the electronic states of the macroscopic system approximately. More specifically, to model an amorphous structure, the KS orbitals are randomly selected and rotated from the MD snapshots of the home cube before placing them into the other cubes. In the same vein, we can model a crystalline structure by letting the KS orbitals be the same in each cube (the polymer chains in each cube can be either warped or straight). Moreover, we can also generate a lamellar structure by keeping the KS orbitals the same in one dimension. In each case, the KS orbitals are used to determine the exciton positions $\mathbf{r}_I$ following Eqs. (7) and (8) in the macroscopic system. The transition rates within each cube (or intracube transition rates) are calculated by Eq. (19) while the intercube transition rates are determined by the distance between the excitons and the relevant intracube transition rates. The rationale behind this approximation and the detailed procedure can be found in Refs. 29 and 30. In this manner, the energies ω_I, positions $\mathbf{r}_I$, and transition rates $\gamma_{I,J}$ for each exciton in the macroscopic system can be obtained.

Exciton diffusion is modeled as random walks using Monte Carlo (MC) simulations. For diffusion of the exciton I, one can generate an event table with $M+1$ transition probabilities (M is the number of excitons considered in the simulation): transition probabilities from the exciton I to $M-1$ neighboring excitons, $P_{1,2,\ldots,M-1} = \gamma_{I,J} \times \Delta t$ with $J = 1, \ldots, I-1, I+1, \ldots, M$; annihilation probability, $P_M = \gamma_{I,0} \times \Delta t$; and the probability to remain at the same state I, $P_{M+1} = 1 - (P_1 + P_2 + \cdots + P_M)$. Δt is the time step of the MC simulations. With these probabilities, a diffusion trajectory of the exciton I is obtained by executing MC moves until the exciton is annihilated. From the trajectory, one can determine the lifetime t (the number of MC moves multiplied by Δt) and the maximum distance $d_{\max}$ of exciton diffusion for each trajectory. Averaging over all trajectories with the same initial exciton position gives the exciton diffusion length, lifetime, and diffusivity by $L_D = \langle d_{\max} \rangle$, $\tau = \langle t \rangle$, and $D = \langle d^2_{\max} \rangle / \tau$, respectively, where the brackets indicate the average. The exciton harvesting efficiency can also be determined from these relevant trajectories as shown in Sec. III B. One can then repeat the same procedure for different excitons.

III. APPLICATION TO CONJUGATED POLYMER P3HT

A. Computational details

Ab initio Born-Oppenheimer molecular dynamics is carried out for the home cube (shown in Fig. 2) of a dimension of 1.8 nm with periodic boundary conditions. The supercell contains 606 atoms, including three P3HT chains each with eight thiophene rings, leading to a mass density of 1.1 g/cm^3, which is similar to the experimental value. The initial structure of the P3HT chains, starting from a randomly placed and warped configuration, is fully relaxed to reach the local energy minimum. The system is brought to a desired temperature by MD with a repeated velocity scaling, and is then kept at the desired temperature for 500 fs with a 1-fs time step to reach the thermal equilibrium. Finally, the microcanonical production MD run is carried out for 1000 fs with a 1-fs time step for each temperature. We have confirmed that the simulated system is equilibrated during the microcanonical MD run.[29] The projector augmented-wave (PAW) pseudopotentials[31] and Perdew-Burke-Ernzerhof (PBE) functional[32] as implemented in the VASP package[33,34] are used in the *ab initio* calculations performed at the Γ point with 300 eV energy cutoff. The six highest occupied KS orbitals and nine lowest unoccupied KS orbitals are included in the Casida's formulation to produce 54 exciton states. In each MD step, we obtain the KS energies and orbitals which are then used to calculate the many-body wave functions and the energies of the 54 excitons.

The entire system of interest consists of $30 \times 30 \times 30$ cubes for which the Monte Carlo simulations are carried out (the dimensions of the simulated system are much larger than the diffusion length, thus are sufficient to represent the realistic macroscopic system). By using different random number sequences, we have constructed 100 different configurations of the entire system. And for each configuration, 100 trajectories of exciton diffusion are modeled by Monte Carlo simulations. In total, we have generated 10^4 trajectories for each initial exciton state considered in the present work. The time step Δt in the Monte Carlo simulations should be chosen judiciously so that $\sum_{m=1}^{M} P_m < 1$ and the minimal time step should be greater than or equal to 1 fs, which is the time step of the MD simulations. We have performed Monte Carlo simulations using $\Delta t = 1$ and 10 fs, respectively, and obtained similar results for the diffusion length and lifetime.

B. Results and discussions

The exciton diffusion consists of interstate transitions (the transitions between two excited states) and annihilations (transitions to the ground state); these transitions can be phonon-assisted or spontaneous. We find that at 300 K the phonon-assisted transition rates range from 10^8 s^{-1} to 10^{13} s^{-1} and from 10^6 s^{-1} to 10^9 s^{-1} for the interstate transitions and annihilations, respectively. The spontaneous emission rates span from 0 to 10^8 s^{-1} and from 10^5 s^{-1} to 10^9 s^{-1} for the interstate transitions and annihilations, respectively. Thus the interstate transitions are dominated by the phonon-assisted processes, while the phonon-assisted and spontaneous transitions contribute equally to the annihilations. From the Fourier transform of the time-dependent exciton energy levels, we can identify the relevant phonon modes that give rise to the exciton-phonon coupling and the nonadiabatic exciton transitions. As shown in Fig. 3, a number of low frequency phonons arising from the bending and torsion modes of the backbones and a much higher frequency phonon from the stretching mode of C=C bonds are responsible for the phonon-assisted exciton dynamics. These results are in excellent agreement with the experimental observations.[35,36]

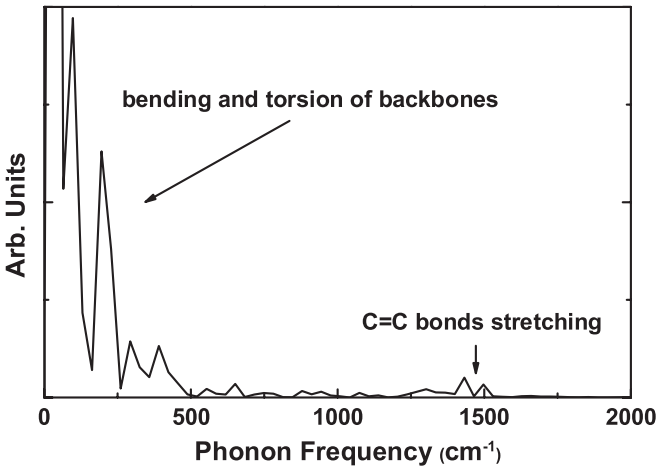

FIG. 3. The Fourier transform of the lowest exciton energy level at 300 K. The frequencies of the bending and torsion modes of the backbones are below 500 cm^{-1}, and the stretching frequency of C = C bonds is about 1500 cm^{-1}.

In the following, we discuss the simulation results of exciton diffusion in amorphous P3HT. Three representative excitons whose initial energies are labeled by $S1$, $S2$, and $S3$ in Fig. 4 are considered. Here the density of states (DOS) counts all possible exciton states at a given energy corresponding to all atomic configurations over the course of MD. $S1$ is at the low-energy tail of the exciton DOS; $S2$ is

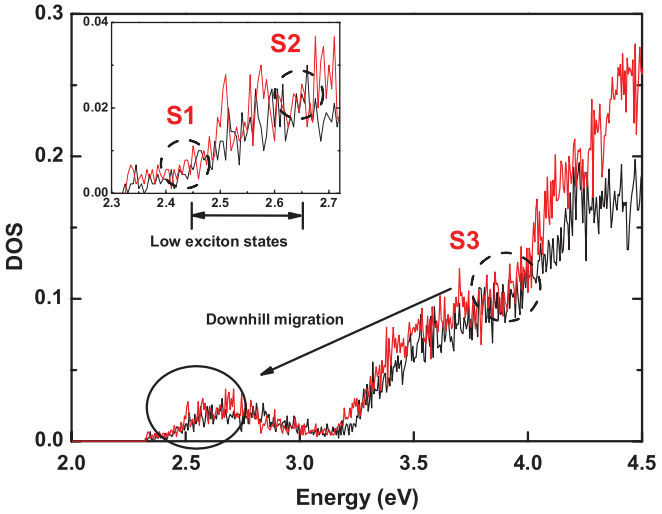

FIG. 4. (Color online) The exciton density of states for 54 excitons (black curve) and 144 excitons (red curve) in each cube at 300 K. Dashed circles show the energy range of $S1$, $S2$, and $S3$ excitons. Inset: A blown-up view of DOS in the energy range indicated by the solid black circle.

TABLE I. Simulated diffusion length L_D (nm), lifetime τ (ns), and diffusivity D (10^{-8} m^2/s) for $S1$, $S2$, and $S3$ excitons at 100, 200, and 300 K, respectively.

	300 K			200 K			100 K		
	$S1$	$S2$	$S3$	$S1$	$S2$	$S3$	$S1$	$S2$	$S3$
L_D	5.1	6.4	7.7	2.9	4.4	6.2	1.7	4.2	6.1
τ	2.3	2.4	2.3	1.8	1.6	1.6	3.6	3.6	3.5
D	1.5	2.1	3.0	0.6	1.4	2.8	0.1	0.6	1.2

0.2 eV higher than $S1$ while $S3$ is 1.5 eV higher than $S1$. While the energy of $S1$ and $S2$ corresponds to the efficient photon adsorption frequencies, the energy of $S3$ approaches the higher limit of the solar spectrum. The results of L_D, τ, and D from the Monte Carlo simulations are summarized in Table I. The experimental values of the exciton diffusion length in P3HT at room temperature scatter considerably: from 2.6–5.3 nm (Ref. 37), 4 nm (Ref. 38), 8.5 nm (Ref. 39), to 27 ± 12 nm (Ref. 40). The corresponding diffusivity ranges from 5×10^{-8} m^2/s (Ref. 38), 2×10^{-7} m^2/s (Ref. 39), to 1×10^{-6} m^2/s (Ref. 40). To understand the large variation of the experimental values, we also consider a crystalline P3HT structure in the Monte Carlo simulations and determine L_D, τ, and D as 17.2 nm, 0.35 ns, and 9×10^{-7} m^2/s, respectively. Clearly the diffusion length and diffusivity in the crystalline P3HT are much higher than those of the amorphous P3HT, and in fact the results are in line with the largest experimental values. Therefore, the exciton dynamics depends sensitively on the structural order of the polymer—more than two orders of magnitude increase in diffusivity can be achieved by improving the structural order. Additionally, the calculated exciton lifetime is ~1 ns, compatible to the experimental values that range from a few hundred ps to ~1 ns (Ref. 41). Finally, it is evident from Table I that the diffusion length and diffusivity increase with the temperature and the exciton with a higher energy has a greater diffusion length and diffusivity.

It has been speculated that exciton diffusion in conjugated polymers is governed by two processes: an initial downhill migration toward lower energies followed by a thermally activated migration.[2,41,42] However, there is no direct evidence that such processes exist and the general behavior of the diffusion processes remains to be understood. Our simulations have unambiguously confirmed that such processes indeed exist and provide a fundamental understanding of the processes. In Fig. 5 we display the evolution of exciton energy vs. diffusion distance for 10^4 trajectories. Each data point corresponds to an MC move with increasing diffusion distance; a positive (negative) ΔE in Figs. 5(a) and 5(c) corresponds to an energy loss (gain). Therefore the initial downhill migration is represented by the red color with positive ΔE, while the thermally activated migration is represented by the yellow and blue colors with oscillating ΔE across the zero energy. The initial downhill migration completes within 10^{-2} ns, much faster than the thermally activated migration (~1 ns). Shown in Fig. 5(b), the downhill process is characterized by a smaller diffusion distance (~5 nm) but with a greater energy loss (>1 eV); in contrast the thermally activated process contributes

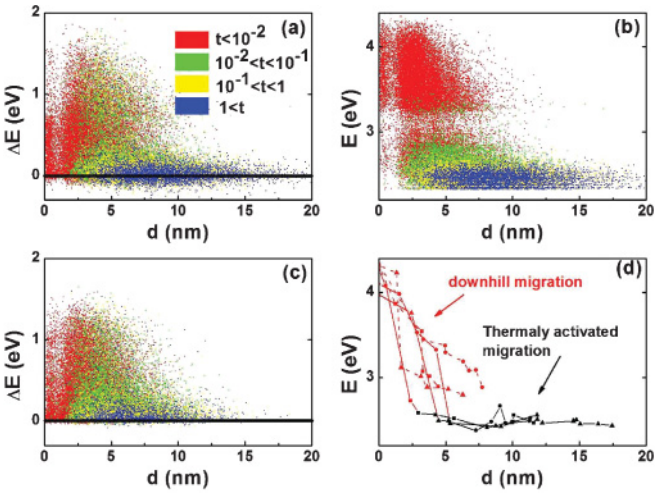

FIG. 5. (Color online) The energy evolution of $S3$ exciton vs. diffusion distance from 10^4 trajectories. (a), (c) The exciton energy difference between two adjacent diffusion moves vs. diffusion distance at (a) 300 and (c) 100 K. The color-coding represents different time ranges; the time is given in ns. (b) The exciton energy vs. the diffusion distance at 300 K. (d) The exciton energy vs. diffusion distance for three randomly selected trajectories at 300 (solid curves) and 100 K (dash curves). The downhill and thermally activated migration processes are represented by the red and black curves, respectively.

to a much longer diffusion distance (up to 20 nm), but with a much smaller energy variation (~0.2 eV). It can also be observed from Fig. 5(b) that the thermally activated process involves exclusively the low-energy excitons that are ~0.2 eV above the lowest exciton energy (i.e., the width of the blue strip is 0.2 eV); these low energy exciton states are also indicated in Fig. 4. By comparing Figs. 5(a) and 5(c), one finds that the thermally activated migration is suppressed at 100 K—there is an absence of energy gain or negative ΔE in Fig. 5(c).

Next, we examine the general behavior of exciton diffusion by focusing on the three representative excitons. Figure 6 shows the percentage distribution of the diffusion distance obtained from 10^4 diffusion trajectories at different temperatures. From Fig. 6 and Table I, we find that (i) the diffusion length increases with temperature for all three excitons, particularly for the low energy excitons such as $S1$; (ii) the diffusion behavior of the higher energy excitons (such as $S2$ and $S3$) is similar at 300 K. These two observations can be understood from the diffusion mechanism outlined above. Since exciton diffusion in real space corresponds to transitions between excited states in energy space, a lower exciton DOS implies fewer possible states for a migrating exciton to make transitions to, hence the diffusion is suppressed. This is the case for $S1$ exciton—the DOS of $S1$ is very small and so is its diffusion length at 100 K. At a higher temperature, however, $S1$ exciton can gain its energy from the phonons promoting $S1$ to a higher energy state with a greater DOS. Hence the diffusion of $S1$ is enhanced by increasing temperature. In contrast, $S3$ can lower its energy via the downhill migration to $S2$. Since the diffusion distance is primarily determined by the thermally activated process, $S3$ has a slightly larger diffusion

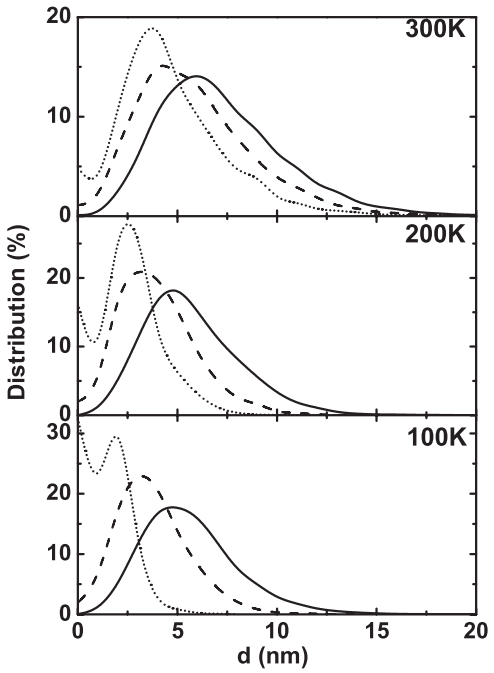

FIG. 6. Statistics (percentage) of exciton diffusion distance for 10^4 exciton diffusion trajectories at 100, 200, and 300 K. Solid, dashed, and dotted curves correspond to $S3$, $S2$, and $S1$ excitons, respectively.

distance than $S2$ (their difference stems from the prior downhill migration from $S3$ to $S2$). Consequently there exists an optimal excitation energy, E_{opt} which is approximately 0.2 eV. The energy of $S2$ is optimal for diffusion; below $S2$, the exciton diffusion at low temperatures is minimal because it has to acquire enough thermal energy for a considerable diffusion distance. On the other hand, a much higher exciton energy does not lead to a much longer diffusion distance because the extra energy will be "lost" to the phonons via inefficient downhill migration.

The diffusion distance distribution shown in Fig. 6 is also useful to estimate exciton harvesting efficiency—an important quantity for photovoltaic performance. For a given diffusion distance r, the integration of the distribution percentage from r to ∞ represents the probability $p(r)$ that an exciton can be harvested. Consider a planar heterojunction in which the P3HT donor layer is sandwiched between two acceptors. Let the exciton be formed at a distance r from the interface and assume the excitons are generated homogeneously in the P3HT layer. The harvesting efficiency can be estimated as $\int_0^L p(r)dr/L$, where L is the thickness of the P3HT layer. At 300 K for the $S3$ exciton, we find that the exciton harvesting efficiency as 90%, 70%, and 10% for $L = 6$, 10, and 70 nm, respectively. In particular, the estimated efficiency of 70% is very close to the experimentally measured photoluminescence quenching efficiency of 68% for P3HT with the same thickness;[43] the corresponding efficiency for the $S2$ exciton is 62%, slightly smaller than the experimental value.

Finally, to verify that 54 excitons in each cube are sufficient to simulate the exciton diffusion in P3HT, we have considered 144 excitons per cube in the simulations—12 highest occupied KS orbitals and 12 lowest unoccupied KS orbitals in Casida's formulation. The values for the diffusion length and diffusivity are practically the same as in the case of 54 excitons. This agreement can be understood from two facts: (1) the DOS below $S3$ is essentially the same for the two cases as shown in Fig. 4 and (2) the DOS above $S3$ is irrelevant to the diffusion. The reason behind the second fact is that the diffusion of the $S3$ exciton proceeds with the downhill migration *initially* as shown in Fig. 5(b), which lowers its energy toward $S2$. The states above $S3$ are not accessed in the diffusion. On the other hand, the energy of the $S1$ and $S2$ excitons is too low to be thermally elevated above $S3$. Therefore 54 excitons per cube are sufficient for the diffusion of the three excitons considered here. In general, the number of excitons in each cube should be determined by ensuring that the DOS below the highest relevant exciton state is correctly reproduced.

IV. CONCLUSION

To conclude, we have developed a computational capability that could potentially guide the rational design of organic optoelectronic materials by predicting exciton dynamics. The theoretical approach is based on first-principles simulations without empirical input. We have studied exciton diffusion in both crystalline and amorphous P3HT conjugated polymers at different temperatures and obtained excellent agreements (including exciton diffusion length, diffusivity, lifetime, and harvesting efficiency) with the experimental results. The simulations unambiguously establish the exciton diffusion mechanism and shed light into the exciton diffusion processes that are difficult to obtain by experiments alone. In addition, the simulations provide the following guidelines that could be potentially useful in materials design. (1) From a structure perspective, exciton diffusion depends sensitively on the crystalline order—a higher structural order renders a greater diffusion length. A more than two orders of magnitude increase in diffusivity can be achieved by optimizing the material structure. (2) From a materials perspective, exciton diffusion depends critically on the electronic density of states near the valence band maximum and conduction band minimum of the semiconductor—a higher density of states near the band edges leads to more low energy exciton states, yielding a greater diffusion length. The optical gap, on the other hand, does not play a role in exciton diffusion. (3) There is an optimal photon frequency for exciton diffusion in each material; therefore in designing tandem solar cells, one should consider frequency dependence both in terms of light adsorption and exciton diffusion in each material to gain the highest overall quantum efficiency.

ACKNOWLEDGMENTS

This work was supported by NSF Solar energy Grants No. DMR-1035480 and No. NSF MRI-R^2 and Grant No. DMR-0958596 for computational facility. We acknowledge discussions with Gui Bazan, Carlos Garcia-Cervera, and Thuc-Quyen Nguyen.

[1] A. C. Mayer, S. R. Scully, B. E. Hardin, M. W. Rowell, and M. D. McGehee, Mater. Today **10**, 28 (2007).
[2] F. B. Dias, K. T. Kamtekar, T. Cazati, G. Williams, M. R. Bryce, and A. P. Monkman, Chem. Phys. Chem. **10**, 2096 (2009).
[3] S. C. J. Meskers, J. Hubner, M. Oestreich, and H. Bassler, J. Phys. Chem. B **105**, 9139 (2001).
[4] C. Madigan and V. Bulovic, Phys. Rev. Lett. **96**, 046404 (2006).
[5] E. Hennebicq, G. Pourtois, G. D. Scholes, L. M. Herz, D. M. Russell, C. Silva, S. Setayesh, A. C. Grimsdale, K. Mullen, J. L. Bredas, and D. Beljonne, J. Am. Chem. Soc. **127**, 4744 (2005).
[6] B. Van Averbeke and D. Beljonne, Chem. Phys. Chem. **10**, 3061 (2009).
[7] M. E. Kose, P. Graf, N. Kopidakis, S. E. Shaheen, K. Kim, and G. Rumbles, Chem. Phys. Chem. **10**, 3285 (2009).
[8] S. Athanasopoulos, E. Hennebicq, D. Beljonne, and A. B. Walker, J. Phys. Chem. C **112**, 11532 (2008).
[9] G. Onida, L. Reining, and A. Rubio, Rev. Mod. Phys. **74**, 601 (2002).
[10] W. R. Duncan, W. M. Stier, and O. V. Prezhdo, J. Am. Chem. Soc. **127**, 7941 (2005).
[11] C. F. Craig, W. R. Duncan, and O. V. Prezhdo, Phys. Rev. Lett. **95**, 163001 (2005).
[12] G. Li, V. Shrotriya, J. S. Huang, Y. Yao, T. Moriarty, K. Emery, and Y. Yang, Nat. Mater. **4**, 864 (2005).
[13] Y. Kim, S. Cook, S. M. Tuladhar, S. A. Choulis, J. Nelson, J. R. Durrant, D. D. C. Bradley, M. Giles, I. McCulloch, C. Ha, and M. Ree, Nat. Mater. **5**, 197 (2006).
[14] J. Yang, R. Zhu, Z. Hong, Y. He, A. Kumar, Y. Li, and Y. Yang, Adv. Mater. **23**, 3465 (2011).
[15] M. Brinkmann and J. C. Wittmann, Adv. Mater. **18**, 860 (2006).
[16] A. J. Moule and K. Meerholz, Adv. Mater. **20**, 240 (2008).
[17] M. E. Casida, *Recent Advances in Density Functional Methods*, edited by D.P. Chong, (World Scientific, Singapore, 1995), pp. 155–192.
[18] H. Iikura, T. Tsuneda, T. Yanai, and K. Hirao, J. Chem. Phys. **115**, 3540 (2001).
[19] Y. Tawada, T. Tsuneda, S. Yanagisawa, T. Yanai, and K. Hirao, J. Chem. Phys. **120**, 8425 (2004).
[20] A. Karolewski, T. Stein, R. Baer, and S. Kummel, J. Chem. Phys. **134**, 151101 (2011).
[21] X. Zhang, Z. Li, and G. Lu (unpublished).
[22] L. M. Blinov, S. P. Palto, G. Ruani, C. Taliani, A. A. Tevosov, S. G. Yudin, and R. Zamboni, Chem. Phys. Lett. **232**, 401 (1995).
[23] P. W. M. Blom, V. D. Mihailetchi, L. J. A. Koster, and D. E. Markov, Adv. Mater. **19**, 1551 (2007).
[24] P. J. Brown, D. S. Thomas, A. Kohler, J. S. Wilson, J. S. Kim, C. M. Ramsdale, H. Sirringhaus, and R. H. Friend, Phys. Rev. B **67**, 064203 (2003).
[25] T. Liu and A. Troisi, J. Phys. Chem. C **115**, 2406 (2011).
[26] C. Hu, H. Hirai, and O. Sugino, J. Chem. Phys. **127**, 064103 (2007).
[27] A. J. Morfa, T. M. Barnes, A. J. Ferguson, D. H. Levi, G. Rumbles, K. L. Rowlen, and J. van de Lagemaat, J. Polym. Sci. Pt. B-Polym. Phys. **49**, 186 (2011).
[28] P. V. Parandekar and J. C. Tully, J. Chem. Phys. **122**, 094102 (2005).
[29] X. Zhang, Z. Li, and G. Lu, Phys. Rev. B **82**, 205210 (2010).
[30] N. Vukmirovic and L. W. Wang, Nano Lett. **9**, 3996 (2009).
[31] P. E. Blochl, Phys. Rev. B **50**, 17953 (1994).
[32] J. P. Perdew, K. Burke, and M. Ernzerhof, Phys. Rev. Lett. **77**, 3865 (1996).
[33] G. Kresse and J. Hafner, Phys. Rev. B **47**, 558 (1993).
[34] G. Kresse and J. Furthmuller, Phys. Rev. B **54**, 11169 (1996).
[35] N. P. Wells and D. A. Blank, Phys. Rev. Lett. **100**, 086403 (2008).
[36] N. Banerji, S. Cowan, E. Vauthey, and A. J. Heeger, J. Phys. Chem. C **115**, 9726 (2011).
[37] J. E. Kroeze, T. J. Savenije, M. J. W. Vermeulen, and J. M. Warman, J. Phys. Chem. B **107**, 7696 (2003).
[38] L. Luer, H. J. Egelhaaf, D. Oelkrug, G. Cerullo, G. Lanzani, B. H. Huisman, and D. de Leeuw, Org. Electron. **5**, 83 (2004).
[39] P. E. Shaw, A. Ruseckas, and I. D. W. Samuel, Adv. Mater. **20**, 3516 (2008).
[40] S. Cook, L. Han, A. Furube, and R. Katoh, J. Phys. Chem. C **114**, 10962 (2010).
[41] I. G. Scheblykin, A. Yartsev, T. Pullerits, V. Gulbinas, and V. Sundstrom, J. Phys. Chem. B **111**, 6303 (2007).
[42] O. V. Mikhnenko, F. Cordella, A. B. Sieval, J. C. Hummelen, P. W. M. Blom, and M. A. Loi, J. Phys. Chem. B **112**, 11601 (2008).
[43] K. M. Coakley, Y. Liu, M. D. McGehee, K. L. Frindell, and G. D. Stucky, Adv. Funct. Mater. **13**, 301 (2003).